Electronic Structure, Chemical Bonding and Electrochemical Characterization of Li_2CuSn_2 and Li_2AgSn_2

Niels Schirmer[a], Florian Winter[b], Samir F. Matar[c], Andrea Balducci[a], and Rainer Pöttgen[b]

[a] Institut für Physikalische Chemie-MEET, Universität Münster, Corrensstrasse 30, 48149 Münster, Germany

[b] Institut für Anorganische und Analytische Chemie, Universität Münster, Corrensstrasse 30, 48149 Münster, Germany

[c] CNRS, Université de Bordeaux, ICMCB, 87 Avenue Dr. A. Schweitzer, 33608 Pessac-Cedex, France

Reprint requests to R. Pöttgen. E-mail: pottgen@uni-muenster.de

Z. Naturforsch. **2014**, *69b*, 1010 – 1020 / DOI: 10.5560/ZNB.2014-4141
Received July 4, 2014

Polycrystalline samples of the stannides Li_2CuSn_2 and Li_2AgSn_2 were obtained by high-frequency melting of the elements in sealed niobium ampoules in a water-cooled sample chamber. Both stannides crystallize with the tetragonal Li_2AuSn_2 type, space group $I4_1/amd$. They are characterized by three-dimensional $[CuSn_2]^{\delta-}$, respectively $[AgSn_2]^{\delta-}$ networks which leave large channels for the lithium ions. Electronic structure calculations show extensive filling of the transition metal *d* bands and residual DOS at the Fermi energy, compatible with metallic character. Calculated Bader charges and the course of the crystal orbital overlap population curves fully support the bonding picture of cationic lithium and a covalently bonded polyanionic network with considerable charge transfer to both, transition metal and tin atoms. Electrochemical investigations have indicated that a reversible insertion and extraction of lithium into the stannides is taking place in the voltage range between 0 and 2.5 V *vs.* Li/Li^+. From CV measurements, the diffusion coefficents of Li_2CuSn_2 and Li_2AgSn_2 were estimated to be in the order of 10^{-14} cm^2 s^{-1}.

Key words: Lithium, Stannides, DFT Calculations, Electrochemistry

Introduction

Binary transition metal (*T*) stannides of nickel and copper have intensively been studied with respect to their solderability for electronic devices and for use as electrode materials for lithium ion batteries. In the course of fundamental research on battery materials especially the iron stannides, as well as Ni_3Sn, Ni_3Sn_4, Cu_3Sn, and Cu_6Sn_5 have been studied with respect to their lithiation behavior [1 – 7]. Lithiation of such binaries can lead to small loading with interstitial lithium with the binary stannide acting as a host structure, or a so-called conversion reaction (a general reaction is $TSn_x + Li \rightarrow LiSn_x + T$) takes place, leaving the transition metal in nano-sized form along with binary lithium stannides.

A parallel approach is the systematic phase-analytical study of the lithium-transition metal-tin phase diagrams, searching for ternary stannides. The crystal chemical data of the various $Li_xT_ySn_z$ stannides have been summarized in review articles along with the results of physical property studies [8, 9]. In all structures the transition metal and tin atoms build up covalently bonded two- or three-dimensional $[T_ySn_z]^{\delta-}$ polyanionic networks which are filled and charge-balanced by the lithium atoms. Systematic ^{7}Li solid-state NMR spectroscopic studies [9] revealed that most of these stannides contain lithium as almost completely oxidized Li^+, underlining the ionic/covalent nature of the chemical bonding between lithium and the polyanion. The highest lithium mobility has been observed for the channel-like polyanions in Li_2TSn_2 phases (T = Cu, Ag, Au) [10 – 12]. Temperature-dependent ^{7}Li NMR spectroscopic studies showed activation energies in the range of 0.29 to 0.47 eV [12]. Parallel electrochemical characterization of Li_2AuSn_2 by GITT and PITT techniques yielded a chemical diffusion coefficient of 1.5×10^{-6} cm^2 s^{-1} [11].

In the course of our systematic studies of chemical bonding and structure-property relationships of lithium transition metal tetrelides and pnictides [13 – 16, and refs. cited therein], we now investigated the bonding peculiarities of the complete series of Li_2TSn_2 (T = Cu, Ag, Au) stannides and studied the electrochemical behavior of Li_2CuSn_2 and Li_2AgSn_2 samples.

Experimental

Synthesis and sample characterization

The Li_2CuSn_2 and Li_2AgSn_2 samples were synthesized directly from the elements. Starting materials were lithium rods (Merck, > 99 %), copper shots (Chempur, 99.999 %), silver granules (Agosi, > 99.9 %), and tin granules (Merck, p. a.). The surface of the lithium rods was first scratched off mechanically. Smaller pieces were cut under dry paraffin oil and subsequently washed with cyclohexane. Both paraffin oil and cylcohexane were dried over sodium wire. The lithium pieces were preserved in Schlenk tubes under argon prior to the reactions. Argon was purified over a titanium sponge (900 K), silica gel, and molecular sieves. The three elements were weighed in the ideal atomic ratio of 2 : 1 : 2 and arc-welded [17] in niobium ampoules under an argon pressure of *ca*. 700 mbar. The ampoules were loaded in a water-cooled quartz sample chamber of an induction furnace (Hüttinger Elektronik, Freiburg, type TIG 2.5/300) [18] and rapidly heated to 1400 K under flowing argon. After 10 min the temperature was lowered at a rate of 100 K min^{-1} to 1100 K for Li_2CuSn_2 and to 900 K for Li_2AgSn_2. These temperatures were kept for another three hours, and the samples were then rapidly cooled by switching off the furnace. The polycrystalline samples could easily be removed mechanically from the metal tubes. The samples are moderately sensitive to moisture and were kept in Schlenk tubes under argon.

The purity of the polycrystalline Li_2CuSn_2 and Li_2AgSn_2 samples was verified through Guinier powder patterns (image plate system Fujifilm, BAS-1800), using Cu$K\alpha_1$ radiation and α-quartz (a = 491.30, c = 540.46 pm) as an internal standard. The experimental patterns were compared to calculated ones [19], using the crystallographic data of the previous structure refinements [12].

Computational details

Two computational methods within the DFT [20, 21] were used in a complementary manner. The Vienna *ab initio* simulation package (VASP) [22 – 24] allows geometry optimization and cohesive energy calculations. For this we use the projector augmented wave (PAW) method [23], with the generalized gradient approximation (GGA) scheme following Perdew, Burke and Ernzerhof (PBE) [25]. Semi-core Li 2*s* states were considered upon building the PAW Li potential. Preliminary calculations with local density approximation LDA [26] led to largely underestimated volumes *versus* the experimental data. The conjugate-gradient algorithm [27] is used in this computational scheme to relax the atoms. The tetrahedron method with Blöchl corrections [28, 29] as well as a Methfessel-Paxton [30] scheme were applied for both geometry relaxation and total energy calculations. Brillouin-zone (BZ) integrals were approximated using the special k-point sampling. The optimization of the structural parameters was performed until the forces on the atoms were less than 0.02 eV Å^{-1} and all stress components less than 0.003 eV Å^{-3}. The calculations converged at an energy cut-off of 500 eV for the plane-wave basis set with respect to the k-point integration up to $8 \times 8 \times 13$ (k_x, k_y, k_z) for best convergence and relaxation to zero strains. The calculations are scalar relativistic and assume spin-degenerate total spins.

Then all-electron calculations with the GGA were carried out for a full description of the electronic structure and the properties of chemical bonding, using the augmented spherical wave (ASW) method devised by Williams, Kübler and Gelatt in 1979 [31] as a linearized method close to the LMTO (Linearized Muffin Tin Orbitals) method. The approach has benefited from continuous developments leading to full potential FP-ASW with implementation of chemical bonding evaluation according to different schemes (*cf.* text book by V. Eyert [32] and references therein). The ASW method uses a minimal basis set for the valence states with the outermost shells representing one of each kind: the valence states and the matrix elements are constructed using partial waves up to $l_{max} + 1 = 3$ for T and Sn and $l_{max} + 1 = 2$ for Li. Sn $4d^{10}$ states lying at low energy ($\sim$ 20 eV below E_F) were considered as core states and not accounted for in the valence basis set. Self-consistency is achieved when charge transfers and energy changes between two successive cycles are below 10^{-8} and 10^{-6} eV, respectively. BZ integrations were performed using the linear tetrahedron method within the irreducible wedge [28, 29]. Besides the site-projected density of states, we discuss qualitatively the pair interactions based on the overlap population analysis with the crystal orbital overlap population approach (COOP) [33]. In the plots, positive, negative and zero COOP indicate bonding, anti-bonding and non-bonding interactions, respectively. Other schemes for analyzing the chemical bonding also exist, such as COHP, based on Hamiltonian populations [34] as well as ECOV (covalent bond energy) based on both COOP and COHP [35].

Electrochemistry

The electrochemically active materials, polycrystalline Li_2AgSn_2 or Li_2CuSn_2, were thoroughly ground, and composite electrodes were prepared by mixing and further grind-

ing 60 wt.-% of the active material with 12 wt.-% conductive carbon (Super C65, TIMCAL) and 28 wt.-% polytetrafluoroethylene (PTFE, Du Pont). The material was rolled out and cut into discs of 1.2 cm diameter which were laminated onto copper discs as current collectors. The electrode mass loading was about 60 mg cm^{-2}.

The electrodes were characterized by X-ray diffraction (CuK_α radiation, Bruker D8 Advance, 2θ range from 20 to 80°) before and after the electrochemical tests. The electrodes were mounted on air- and water-tight sample holders in an argon-filled glove box. The cycled electrodes were washed three times with DMC to remove traces of the solvents and the lithium salt $LiPF_6$.

Electrochemical tests were carried out in Swagelok®-type 3-electrodes cells, which were assembled in an argon-filled glove box ($H_2O < 1$ ppm, $O_2 < 1$ ppm). For all experiments, a Whatman GF/D glass microfiber filter of 675 μm in thickness and 12 mm in diameter was used as a separator. The separator was drenched with 120 μL of 1 M $LiPF_6$ in ethylene carbonate-dimethyl carbonate (EC-DMC) 1 : 1.

The electrodes were tested in half-cell configuration, using metallic lithium as counter and reference electrodes. All electrochemical tests were performed at 20 °C in a climate chamber using a VMP multichannel potentiostatic-galvanostatic system (BioLogic Science Instruments, Claix, France).

Cyclic voltammetry (CV) was carried out in the voltage range from 0 to 2.5 V *vs.* Li/Li^+. At first 5 cycles at a scan rate of 0.1 mV s^{-1} were performed followed by 6 cycles each at a different scan rate (0.01, 0.02, 0.05, 0.1, 0.2, and 0.5 mV s^{-1}).

Constant current (CC) tests were performed applying a charge-discharge current of C/5. A theoretical capacity of 100 mAh g^{-1} was assumed and used for the calculation of the current density.

For the GITT experiments short current pulses of current densities corresponding to a C-rate of C/5 were applied for 10 min, followed by a relaxation time of 2 h to allow the system to achieve electrochemical equilibrium.

All potentials are referred to the potential of the redox couple of lithium metal Li/Li^+ in contact with the 1 M $LiPF_6$ containing the electrolyte EC/DMC.

Discussion

Crystal chemistry

Before we start discussing the chemical bonding peculiarities and the electrochemical behavior of these stannides, we briefly recall their crystal chemistry, exemplarily for Li_2CuSn_2 [12]. A view of the crystal structure approximately along the crystallographic *b* axis is presented in Fig. 1. The structure has a simple monomeric building unit. Each copper atoms is tetrahedrally coordinated by four tin atoms at Cu–Sn distances of 264 pm, close to the sum of the covalent radii for Cu + Sn of 257 pm [36]. These tetrahedra share common corners within the crystallographic *ab* plane, and the resulting layers of tetrahedra are condensed in *c* direction *via* Sn–Sn bonds in such a way that zig-zag chains are formed. Due to the space group symmetry, these zig-zag chains extend in *a* as well as in *b* direction. This connectivity pattern leads to a three-dimensional $[CuSn_2]^{\delta-}$ polyanionic network which leaves diverse channels for the lithium cations.

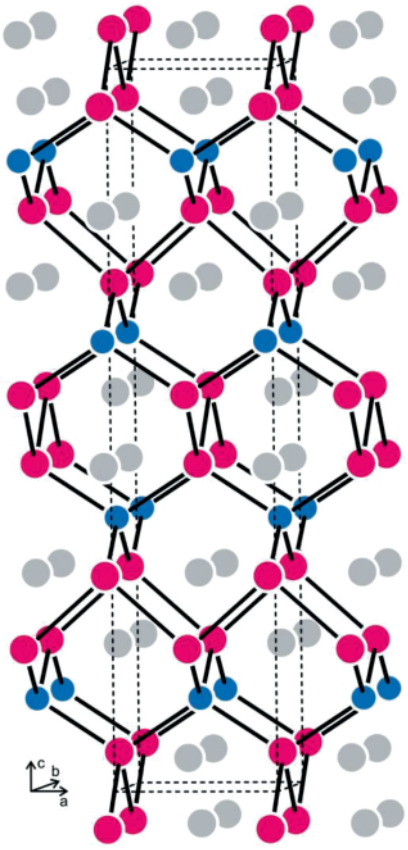

Fig. 1 (color online). The crystal structure of Li_2CuSn_2 (Li_2AuSn_2 type, $I4_1/amd$). Lithium, copper and tin atoms are drawn as light grey, blue and magenta circles, respectively. The three-dimensional $[CuSn_2]^{\delta-}$ polyanionic network is emphasized.

The Sn–Sn zig-zag chains show Sn–Sn distances of 296 pm, shorter than the Sn–Sn distances of 4×302

and 2×318 pm in the β-Sn structure [37]. Although the structure consists of a simple basic building unit, the bonding pattern is not that simple. The temperature-dependent solid-state NMR spectra indicate almost fully ionized Li^+ in all three Li_2TSn_2 (T = Cu, Ag, Au) stannides [10, 12]. According to the Zintl-Klemm concept, a zig-zag chain of tin atoms is expected for a Sn^{2-} species, similar to CaSn [38] with a 290 pm Sn–Sn distance. Keeping the monovalent nature of lithium in mind, a Zintl-conform electron partitioning would force the transition metal to a divalent state. This is highly improbable at least for silver and gold and furthermore, a paramagnetic state in the case of Cu(II) would have hampered the solid-state NMR spectroscopic studies. The situation of chemical bonding in these stannides is elucidated in more detail in the following.

Electronic structure and chemical bonding

The geometry-optimized crystal structure results (Table 1) are in relatively good agreement with the experimental data especially for z_{Li} and z_{Sn} in all three compounds though larger volumes were obtained due to the use of the GGA approximation accounting for the exchange correlation effects in the DFT, the GGA functional being known to be 'underbinding' (*versus* LDA). Then the results can be used to examine energy trends and charge transfers. The cohesive energies of the three compounds can be obtained from the difference between the total electronic energy at self-consistent convergence on one hand and those of the constituents Li, T and Sn in their ground state crystal structures on the other : $E_{coh}(Li_2TSn_2) = E_{total}(Li_2TSn_2) - \Sigma\ E_{total}(2Li,\ T,\ 2Sn)$ for one formula unit (FU). The calculations are explicitly carried out for 2 FUs. The energies (eV) of the respective atomic constituents are as follows: E(Li, bcc) = −1.902; E(Cu, fcc) = −3.714; E(Ag, fcc) = −2.772; E(Au, fcc) = −3.212; E(Sn, tetragonal β-modification) = −3.746.

Table 1. Experimental and calculated (in parentheses) crystal data for the stannides Li_2TSn_2 (T = Cu, Ag, Au), space group $I4_1/amd$. Atomic positions: T at 4*b* (1/2, 1/4, 1/8); Li, Sn at 8*e* (0, 1/4, *z*). Li_2CuSn_2: a = 442.6 (445.6), c = 1940.9 (1949.9) pm, V = 0.3802 (0.3872) nm^3; Li_2AgSn_2: a = 456.3 (463.8), c = 2018.2 (2010.5) pm, V = 0.4203 (0.4325) nm^3; Li_2AuSn_2: a = 455.6 (461.7), c = 1957.4 (1989.4) pm, V = 0.4063 (0.4241) nm^3.

	Li_2CuSn_2	Li_2AgSn_2	Li_2AuSn_2
z_{Li}	0.549 (0.548)	0.549 (0.549)	0.551 (0.551)
z_{Sn}	0.0506 (0.052)	0.0462 (0.047)	0.0484 (0.048)

Taking into account the respective multiplicities, the resulting cohesive energies are:

$$E_{coh}\,(Li_2CuSn_2) = -1.72 \text{ eV per FU};$$
$$E_{coh}\,(Li_2AgSn_2) = -1.83 \text{ eV per FU};$$
$$E_{coh}\,(Li_2AuSn_2) = -2.52 \text{ eV per FU}.$$

The results indicate an increasingly larger cohesion of the structure along the T series under inspection. This suggests that the trend for Li de-intercalation should be increasingly difficult along the T = Cu, Ag, Au series. The differences in total energy between the compound on one hand and its Li-vacant homolog and atomic Li on the other then give a hint for the energy required for lithium removal. Note that this should merely show the trends of Li mobility:

$$\Delta E = E_{tot}\,(Li_2TSn_2) - E_{tot}\,(\text{Li-vacant}) - nE_{Li}$$

where n = number of Li atoms per FU.

The resulting magnitudes are

$$\Delta E_{Li}(T = \text{Cu}) = -0.991 \text{ eV}$$
$$\Delta E_{Li}(T = \text{Ag}) = -1.005 \text{ eV}$$
$$\Delta E_{Li}(T = \text{Au}) = -1.245 \text{ eV}.$$

The evolution of ΔE_{Li} follows from the trend of the cohesive energies shown above. Although close energy values are found for the three compounds, the trend is towards increasing absolute values in the series. The potentials for full removal of Li (working hypothesis) are obtained by opposite signs. These magnitudes are larger than in the binary silicide $Li_{15}Si_4$ which is characterized by a potential of 0.30 V [39] and smaller than those calculated formerly for the ternaries $LiCo_6P_4$ and $Li_2Co_{12}P_7$ with respectively 1.71 V and 1.73 V [15] as well as for the equiatomic silicide LiYSi with 1.69 V [40]. It needs to be mentioned that contrary to the above-cited lithium ternaries, the full geometry relaxation calculations for the Li-free compounds led to large changes in the crystal structures especially for the c lattice parameters. In this model, upon removal of all Li atoms one is left with TSn_2 binaries, with $AuSn_2$ being known in a *Pbca* orthorhombic structure [41], it becomes relevant to carry out

Table 2. Experimental and calculated crystal parameters of $AuSn_2$ in hypothetical de-intercalated Li_2AuSn_2 and in its actual orthorhombic structure.

$I4_1/amd$, $Z=4$	$2\square_{Li}AuSn_2$ (calcd.)	
a, pm	488	
c, pm	1520	
Volume, nm^3	0.3612	
Sn (8*e*) 0, 1/4, z	$z=0.053$	
d_{Au-Sn}, pm	267	
Energy per 2 FUs, eV	−21.44	
Energy per unit cell (8 FU):	−85.76 eV	
Pbca, $Z=8$	$AuSn_2$ [41]	$AuSn_2$ calcd.
a, pm	689.8	701.5
b, pm	701.1	715.5
c, pm	1177.3	1189.4
Volume, nm^3	0.5694	0.6014
Au (8*c*) x,y,z	0.01177(3)	0.013
	0.89185(3)	0.891
	0.11650(2)	0.116
Sn1 (8*c*) x,y,z	0.85258(5)	0.853
	0.25116(6)	0.252
	0.08937(4)	0.092
Sn2 (8*c*) x,y,z	0.12914(5)	0.130
	0.52783(6)	0.530
	0.17234(3)	0.173
d (Au–Sn1), pm	272	277
d (Au–Sn2), pm	273	278
Energy, eV per 8 FUs		−90.83

a comparative study of the energetics between the de-intercalated "$2\square_{Li}AuSn_2$" and $AuSn_2$.

Table 2 summarizes the results showing mainly three aspects: the metastable state of de-intercalated Li_2AuSn_2 in as far as $\Delta E \sim 5$ eV per cell difference is obtained with respect to $AuSn_2$ [41], the d_{Au-Sn} distance which tends to be smaller (267 pm) with respect to the average Au–Sn separation of 280 pm, and finally the very large volume difference between the metastable binary (0.0903 nm^3 per FU) and $AuSn_2$: (calcd.: ~ 0.075 nm^3 per FU and exp.: 0.071 nm^3 per FU). It may be suggested that a full de-intercalation is unlikely due to the destabilization of the metal substructure.

The electron transfer behavior can be derived from charge density analyses using the AIM (atoms in molecules theory) approach [42]. Typically, the charge density in a chemical bond reaches a minimum between two different atoms, and this is a natural region to separate them from each other. Such an analysis does not constitute a tool for evaluating absolute ionizations but allows to establish trends between similar chemical systems. For the three compounds the average charge values (Q) are:

$$\begin{aligned} Li_2CuSn_2:\ & Q(Li) = +0.84 \qquad Q(Cu) = -0.82 \\ & Q(Sn) = -0.43 \\ Li_2AgSn_2:\ & Q(Li) = +0.85 \qquad Q(Ag) = -0.95 \\ & Q(Sn) = -0.38 \\ Li_2AuSn_2:\ & Q(Li) = +0.81 \qquad Q(Au) = -1.22 \\ & Q(Sn) = -0.20 \end{aligned}$$

For T the trend of charge transfer follows the electronegativity values: $\chi Cu = 1.90$; $\chi Ag = 1.94$ and $\chi Au = 2.24$. The tendency is towards a decreasing charge on Sn while the charge on Li remains close to $\sim +0.8$, with the lowest for Li_2AuSn_2. The charge distribution differs from the simple Zintl-Klemm-type approximation discussed above.

Using the experimental data given in Table 1 further detailed calculations of the electronic structure and bonding with the scalar relativistic ASW method were carried out. At self-consistent convergence of the energies and charges, small trends of charge transfers similar to the above ones were obtained. The site-projected density of states PDOS values are shown in Fig. 2. The energy reference along the a axis is with respect to the Fermi level E_F. Due to the large filling of the T elements belonging to the end of the *nd* series ($n=3$, 4, 5) Cu, Ag and Au d-PDOS are found within the valence band (VB) well below E_F. The itinerant states are found on both sites of the d states showing similar shapes for the s and p states of Li and Sn. This reflects the chemical bonding between the different constituents ensuring the cohesion of the crystal structure especially for Au–Sn as shown here below. However, the lowest and highest parts of the valence band are characterized by Sn s and p states with relatively high participation exhibiting respectively little and significant similarities with Au and Li states. This arises from the atomic ratio of Sn *versus* Au on one hand (2 : 1) and is also due to the fact that Li participates only with its s like valence states.

The chemical bonding is discussed based on the overlap population analysis using the COOP criterion (Fig. 3). The VB is of mainly bonding character (positive COOP magnitudes) except near the top of the VB due to T–Sn bonding which shows the peculiar characteristics of nearly unique bonding under the d PDOS. These COOPs are followed by intense Li–Sn bonding near the top of the VB whereas only negligible Li–T bonding can be traced. These differences follow from the distances $d(T\text{–Sn}) \sim 270$ pm and d(Li–Sn)

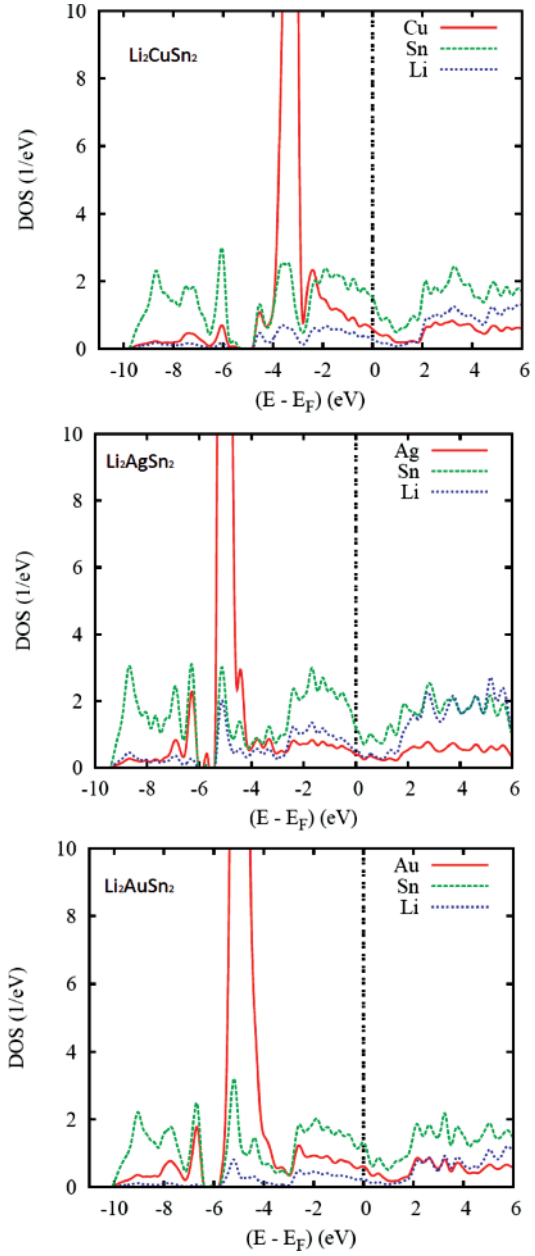

Fig. 2 (color online). Site-projected density of states of the stannides Li_2TSn_2.

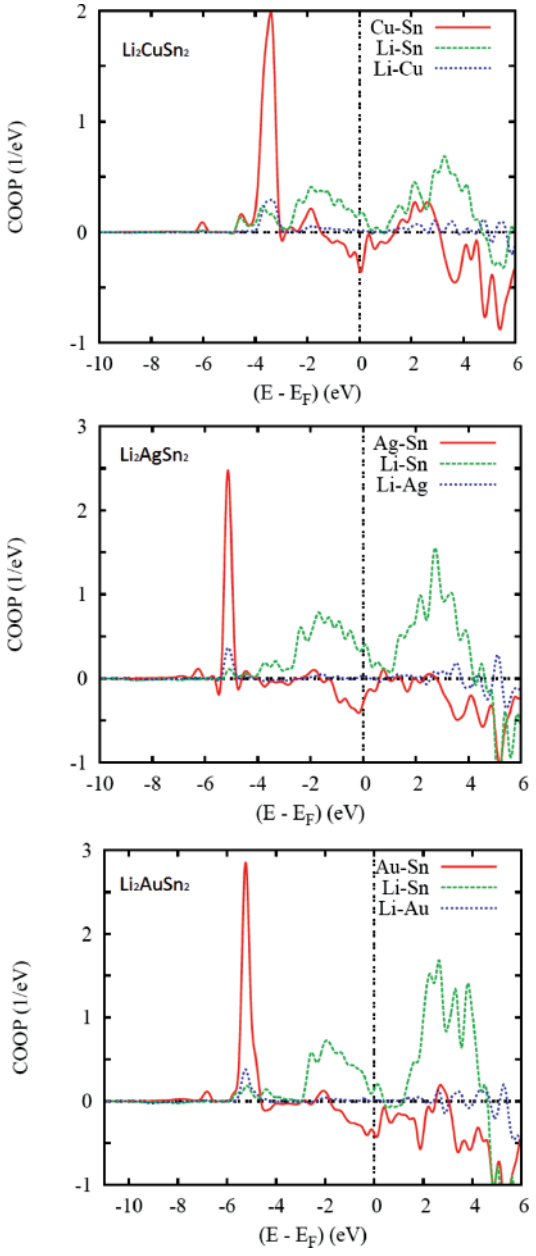

Fig. 3 (color online). Chemical bonding for pair interactions in the stannides Li_2TSn_2.

~ 290 pm. Although the distances $d(T\text{–Li}) \sim 270$ pm are relatively short, only weak bonding can be identified. This is mainly caused by the valence states available for the bonding, *i. e.* s, p (Sn) with s, p (Li). Note that the s electronic charge of Li is redistributed over p and d states thanks to the quantum mixing with neighboring 'ligands'.

Lastly in view of the Sn–Sn zig-zig chains with short Sn–Sn distances (290 pm) we show the Sn–Sn bonding in the three compounds in Fig. 4. The Sn–Sn interac-

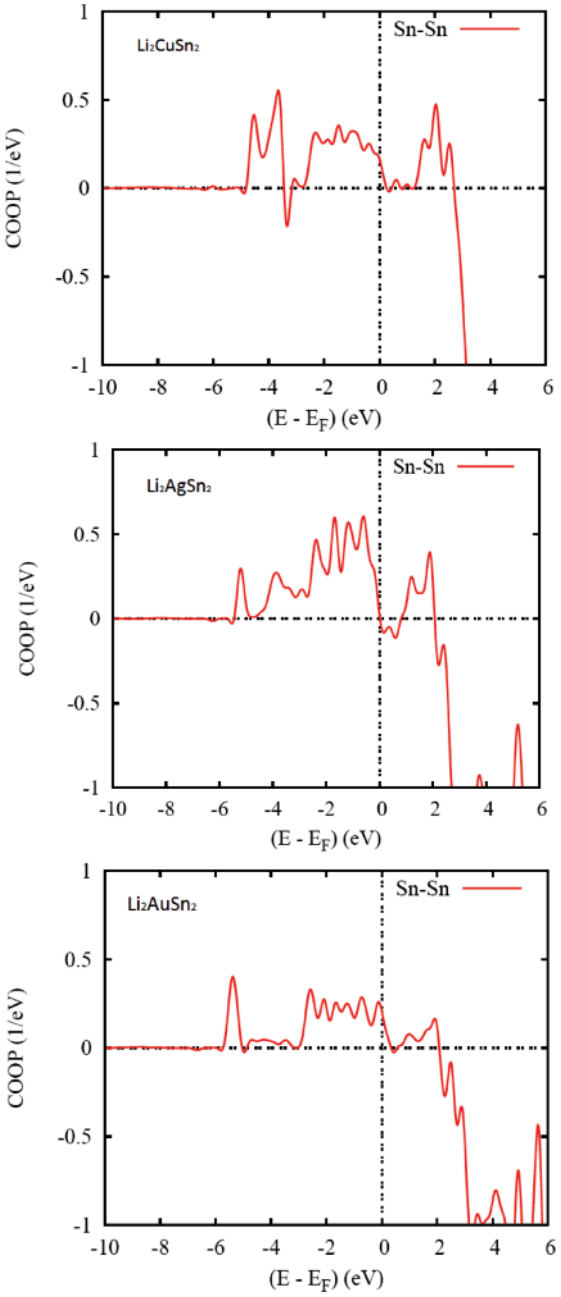

Fig. 4 (color online). Chemical bonding for Sn–Sn interactions in the stannides Li_2TSn_2.

tion is of bonding type with positive COOP magnitudes within the VB. It is also bonding within the CB up to ~ 2 eV and then becomes strongly anti-bonding. With respect to the COOP in Fig. 3, the Sn–Sn COOPs are of similar magnitudes as Li–Sn so that they contribute significantly to the cohesion of the structure.

Electrochemical studies

Fig. 5 shows powder XRD data obtained from the Li_2CuSn_2 and Li_2AgSn_2 electrodes prior and after electrochemical tests (GITT measurements) of the duration of about 200 h. The XRD patterns of the electrodes in Figs. 5a and 5b prior to cycling fit well with the single-crystal data of the pure compounds [12]. The observed mismatch in intensity may be due to inhomogeneity of the prepared electrodes, which may contain larger particles with a certain preferred orientation. After the GITT measurement (for detail see Experimental) the electrodes were washed to remove any remaining traces of electrolyte and mounted on air- and moisture-tight sample holders in a glove box. Although air and moisture contact was prevented, the electrodes showed markedly changed XRD patterns which indicated a decomposition of the active materials within the electrodes. Both types of electrodes show a strong decrease of the reflection intensities of Li_2CuSn_2 and Li_2AgSn_2, while other reflections have emerged. In Figs. 5c and 5d the XRD powder data of the aged electrodes after cycling are compared to the reflections of possible decomposition products. The data indicate that a large fraction of the Li_2CuSn_2 in the electrode clearly was converted to metallic Sn and metallic Cu. The electrode which contained Li_2AgSn_2 displays a similar behavior. The major decomposition product is again metallic Sn and in addition metallic Ag.

Nevertheless, an electrochemical characterization of the stannides Li_2CuSn_2 and Li_2AgSn_2 has been achieved. In order to provide an overview over the electrochemical activity of the two compounds the electrodes were subjected to CVs starting from open-circuit potential (OCP) and going to vertex potentials 0 and 2.5 V *vs.* Li/Li^+ with a high scan rate of 0.1 mV s^{-1}. Fig. 6 shows the cycles 1, 3 and 5 of these CV experiments. It is evident that the OCP of Li_2CuSn_2 (Fig. 6a) is about 0.91 V while Li_2AgSn_2 (Fig. 6b) shows a value of about 0.85 V (close to the calculated values mentioned above). These values have also been confirmed by the OCP periods prior to other electrochemical experiments on the materials. The CVs furthermore indicate that a certain activation process of the material takes place in the initial cycles, which results in the increase of the specific

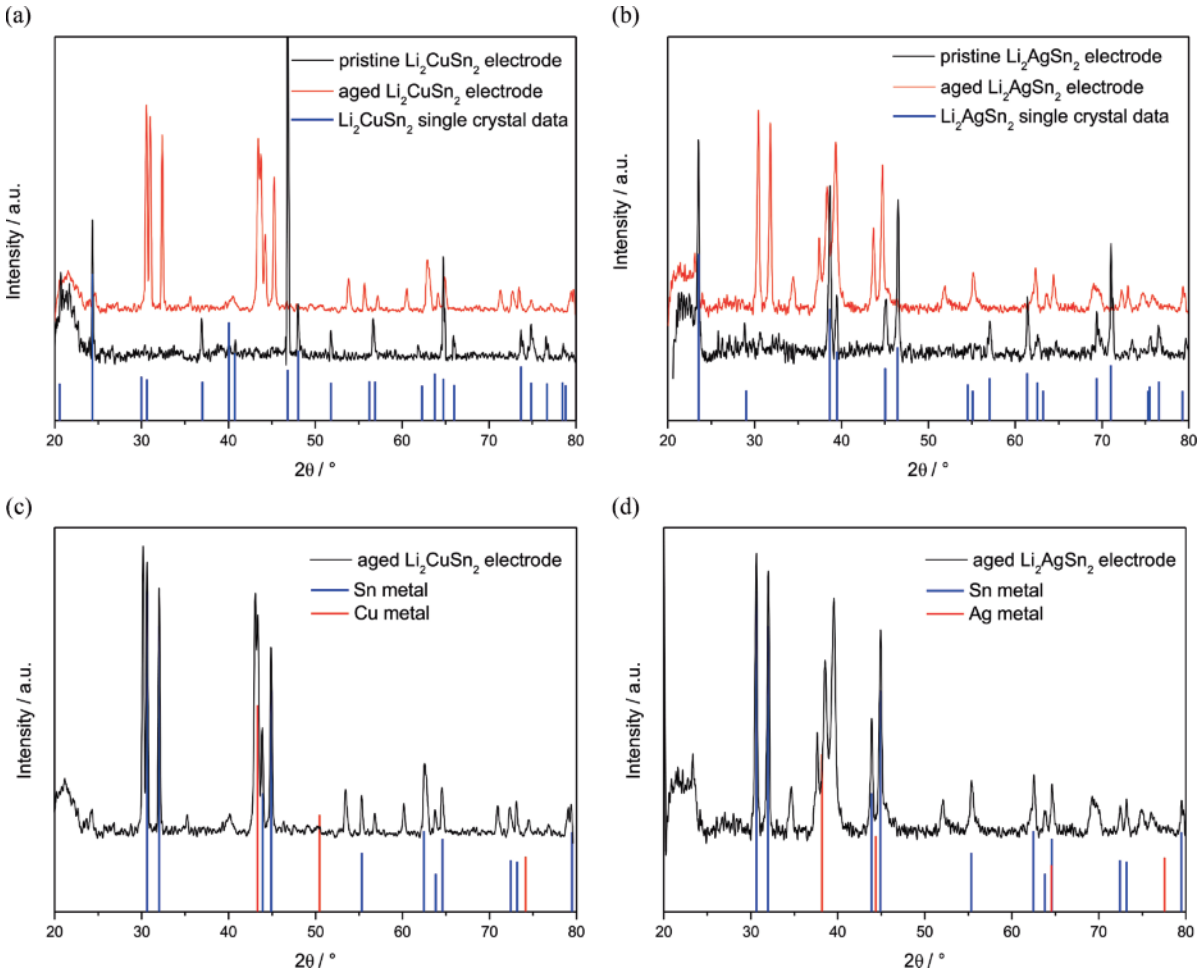

Fig. 5 (color online). PXRD patterns of composite electrodes containing Li_2CuSn_2 and Li_2AgSn_2 as the active materials: (a) pristine Li_2CuSn_2-based electrode; (b) pristine Li_2AgSn_2-based electrode; (c) aged Li_2CuSn_2-based electrode, and (d) aged Li_2AgSn_2-based electrode.

current of the peaks displayed in the CVs. Such a behavior has already been reported in an earlier publication dealing with the electrochemistry of Li_2AuSn_2 which shows isotypy to the materials examined in this study [11, 12].

There are strong similarities in the electrochemical response in the CVs of the electrodes prepared from the stannides Li_2CuSn_2, Li_2AgSn_2 and Li_2AuSn_2 with nano-structured Sn-based electrodes [43]. Complementary to the XRD data, this leads to the conclusion that a certain part of the electrochemical activity of these compounds is due to their decomposition products which are mainly metallic Sn and metallic Cu or Ag or binary compounds like Li_xSn_y. This behavior is similar to the typical conversion reactions observed for many active battery materials [44].

In order to characterize the lithium mobility of Li_2CuSn_2 and Li_2AgSn_2, the lithium diffusion coefficients were determined *via* CVs at scan rates between 0.01 and 0.5 mV s^{-1} as shown in Figs. 6c and 6d. The CVs used to determine the chemical lithium diffusion coefficient were carried out after the five CVs during which activation and conversion of the materials occurred to avoid any influence of this activation process on the diffusion measurements.

The obtained data were used to determine the diffusion coefficients at the peak positions *via* the Randles-Sevcik equation:

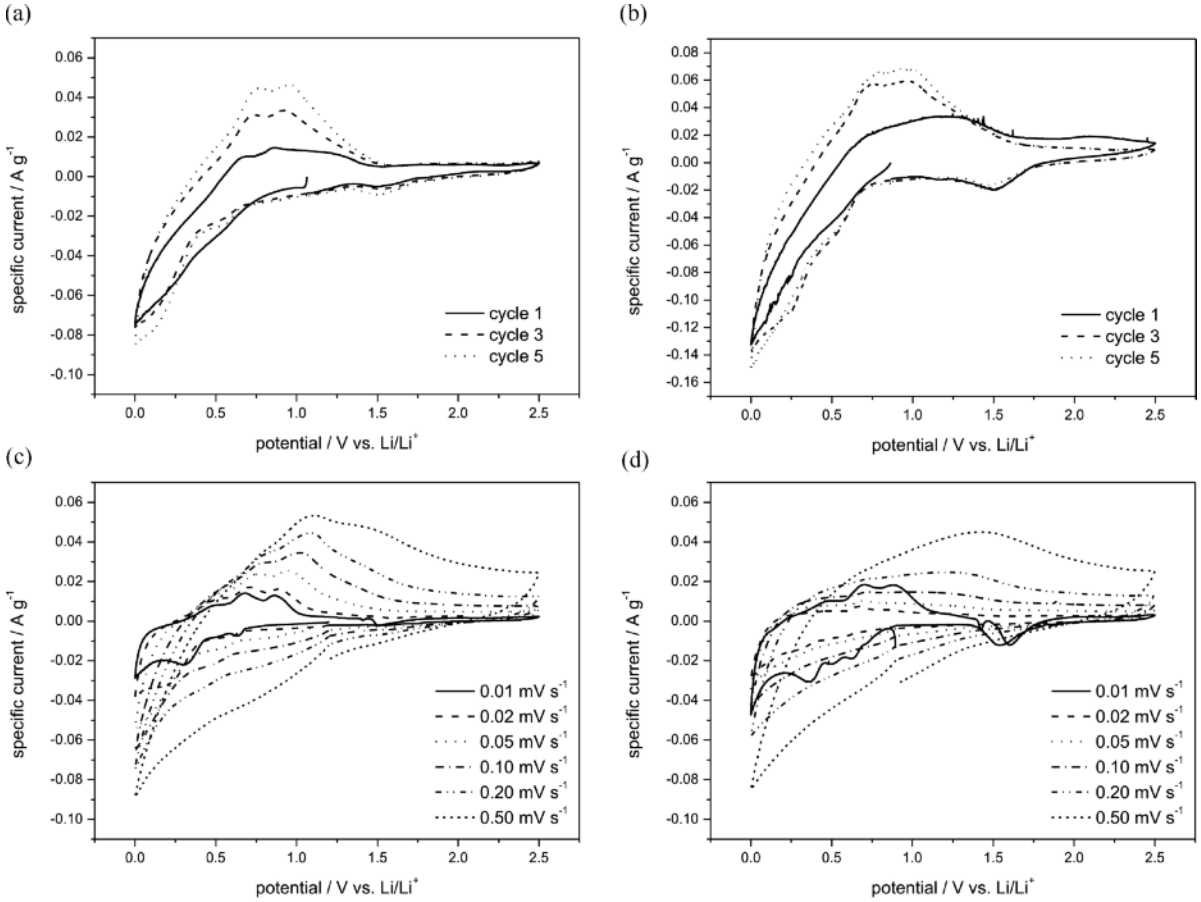

Fig. 6. CV of composite electrodes containing Li_2CuSn_2 and Li_2AgSn_2 as the active materials in the voltage range between 0 and 2.5 V *vs.* Li/Li^+: (a) CV of an Li_2CuSn_2-based electrode at the scan rate of 0.1 mV s^{-1}; (b) CV of an Li_2AgSn_2-based electrode at the scan rate of 0.1 mV s^{-1}; (c) CVs of an Li_2CuSn_2-based electrode at scan rates between 0.01 mV s^{-1} and 0.5 mV s^{-1}, and (d) CVs of an Li_2AgSn_2-based electrode at scan rates between 0.01 mV s^{-1} and 0.5 mV s^{-1}.

$$i_p = kn^{3/2} A\, D_0^{1/2} C_{Li^+}\, \nu^{1/2} \quad (1)$$

The constant k has a value of 2.69×10^5 C mol^{-1} $V^{-1/2}$ under standard conditions (25 °C). The other parameters were determined by taking into account the experimental setup and the material properties (number of electrons n involved in the process, electroactive area A (1.13 cm^2 geometric surface area of the electrodes), lithium ion concentration C_{Li^+} (Li_2CuSn_2 8.74×10^{-3} mol cm^{-3}, Li_2AgSn_2 7.91×10^{-3} mol cm^{-3}) potential scan rate ν (V s^{-1}), and peak current i_p (A). The peak current i_p increases with the square root of the potential scan rate ν. By plotting the slope of the peak current i_p *versus* the square root of the scan rate ν the diffusion coefficient can be determined from the slope of this linear. Since the relation between potential and time of current pulse $\tau^{1/2}$ follows a straight line, Eq. 1 can be applied for the calculation of the lithium ion diffusion coefficients.

The CVs of the Li_2CuSn_2 electrodes (Fig. 6c) show the expected increase of the peak current with increasing scan rate. In contrast, the CVs of the Li_2AgSn_2 electrodes (Fig. 6d) feature very distinct and clear peaks at the lowest scan rate of 0.01 mV s^{-1} but seem to deteriorate at about 1.5 V resulting in strongly decreased peak currents in the following cycles. The diffusion coefficients determined from the two oxidative peaks A and B at 0.68 and 0.85 V, respec-

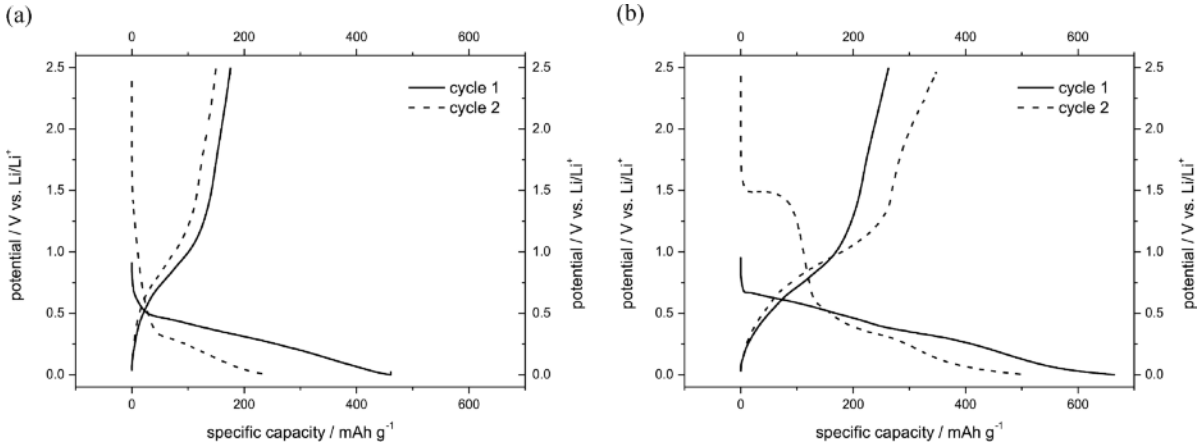

Fig. 7. Voltage profile of electrodes containing (a) Li_2CuSn_2 and (b) Li_2AgSn_2 as the active materials in the voltage range between 0 and 2.5 V *vs.* Li/Li^+. The tests were carried out using a C-rate of $C/5$.

tively, in the CVs of Li_2CuSn_2 are 9.7×10^{-14} cm^2 $s^{-1}$and 1.6×10^{-13} cm^2 s^{-1}, respectively. As a result of the strong deterioration of the peak intensities of Li_2AgSn_2 a more reliable determination of the diffusion coefficients is not possible. Nevertheless, it is important to remark that the determined values are in the same order of magnitude as those derived from the temperature-dependent ^7Li solid state NMR spectroscopic data [12].

Finally, in order to examine how much charge, respectively equivalents of lithium the materials are able to accept and release during constant-current experiments fresh cells were subjected to charge-discharge experiments. The electrodes were galvanostatically cycled in the potential range of 0 to 2.5 V at a C rate of $C/5$. The theoretical specific capacity was based on the results of previous experiments on the isotypic stannide Li_2AuSn_2. The first charge of the Li_2CuSn_2 electrode provides a specific capacity of 457 mAh g^{-1}, but the following discharge gives only 157 mAh g^{-1} (Fig. 7a). This large difference between charge and discharge results in a low efficiency of 34 %, already indicating a highly irreversible capacity. This irreversible capacity cannot solely be attributed to electrolyte decomposition but rather indicates a partial decomposition of the active material Li_2CuSn_2. The second charge-discharge cycle features an improved but still unsatisfactory efficiency of about 61 %. The first charge of the Li_2AgSn_2 electrode results in a specific capacity of 663 mAh g^{-1} and the discharge in a specific capacity of 263 mAh g^{-1} (Fig. 7b). The efficiency of 39 % is similar to that of the Li_2CuSn_2 electrodes. Furthermore, the efficiency of 69 % is comparable to that of the Li_2CuSn_2 material, and the charge capacity is significantly reduced in the second cycle. In contrast to the Li_2CuSn_2 electrodes the discharge capacity in the second cycle is not reduced but increases from 263 to 353 mAh g^{-1}. This increased discharge capacity may be related to the decomposition of the Li_2AgSn_2 material and the formation of metallic Sn and binary Li_xSn_y phases. Sn is known to be a high-capacity anode material for lithium ion batteries with a low initial efficiency [45]. A further indication of the irreversible transformation is the plateau at about 1.5 V in the second cycle which corresponds well to the peak observed in the first CV at 0.01 mV s^{-1} of the Li_2AgSn_2 electrode.

Acknowledgement

This work was financially supported by the Deutsche Forschungsgemeinschaft and the Conseil Régional d'Aquitaine. A. Balducci thanks the University of Münster and the Ministry of Innovation, Science and Research of North Rhine-Westphalia (MIWF) within the project "Superkondensatoren und Lithium-Ionen-Hybrid-Superkondensatoren auf der Basis ionischer Flüssigkeiten" for the financial support. Computational facilities provided by the MCIA-Université de Bordeaux cluster are acknowledged.

[1] C. J. Evans, Tin Handbook, 3rd edition, Hüthig, Heidelberg, **1994**.
[2] M. Winter, J. O. Besenhard, *Electrochim. Acta* **1999**, *45*, 31.
[3] M.-Z. Xue, Z.-W. Fu, *Solid State Ionics* **2006**, *177*, 1501.
[4] N. Dimov in *Lithium-Ion Batteries – Science and Technologies*, Springer, (Eds.: M. Yoshio, R. J. Brodd, A. Kozawa), New York, **2009**, chapter 11, pp. 241 – 265.
[5] K. E. Aifantis in *High Energy Density Lithium Batteries*, (Eds.: K. E. Aifantis, S. A. Hackney, R. V. Kumar), Wiley-VCH, Weinheim, **2010**, chapter 6, pp. 129 – 164.
[6] A. D. W. Todd, P. P. Ferguson, M. D. Fleischauer, J. R. Dahn, *Int. J. Energy Res.* **2010**, *34*, 535.
[7] T. Osaka, H. Nara, H. Mukaibo in *Nanomaterials for Lithium-Ion Batteries – Fundamentals and Applications*, (Ed.: R. Yazami), CRC Press, Taylor and Francis Group, Boca Raton, **2014**, chapter 3, pp. 95 – 139.
[8] R. Pöttgen, Zh. Wu, R.-D. Hoffmann, G. Kotzyba, H. Trill, J. Senker, D. Johrendt, B. D. Mosel, H. Eckert, *Heteroatom Chem.* **2002**, *13*, 506.
[9] R. Pöttgen, T. Dinges, H. Eckert, P. Sreeraj, H.-D. Wiemhöfer, *Z. Phys. Chem.* **2010**, *224*, 1475.
[10] Zh. Wu, B. D. Mosel, H. Eckert, R.-D. Hoffmann, R. Pöttgen, *Chem. Eur. J.* **2004**, *10*, 1558.
[11] P. Sreeraj, N. A. Kaskhedikar, H.-D. Wiemhöfer, J. Maier, R. Pöttgen, *Solid State Ionics* **2010**, *181*, 59.
[12] F. Winter, S. Dupke, H. Eckert, U. Ch. Rodewald, R. Pöttgen, *Z. Anorg. Allg. Chem.* **2013**, *639*, 2790.
[13] T. Langer, S. Dupke, H. Eckert, S. F. Matar, M. Winter, R. Pöttgen, *Solid State Sci.* **2012**, *14*, 367.
[14] S. F. Matar, R. Pöttgen, A. F. Al Alam, N. Ouaini, *Chem. Phys. Lett.* **2012**, *542*, 47.
[15] S. F. Matar, A. Al-Alam, N. Ouaini, R. Pöttgen, *J. Solid State Chem.* **2013**, *202*, 227.
[16] F. Winter, R. Pöttgen, M. Greiwe, T. Nilges, *Rev. Inorg. Chem.* **2014**, *34*, in press. doi:10.1515/revic-2014-0003.
[17] R. Pöttgen, T. Gulden, A. Simon, *GIT Labor-Fachzeitschrift* **1999**, *43*, 133.
[18] D. Kußmann, R.-D. Hoffmann, R. Pöttgen, *Z. Anorg. Allg. Chem.* **1998**, *624*, 1727.
[19] K. Yvon, W. Jeitschko, E. Parthé, *J. Appl. Crystallogr.* **1977**, *10*, 73.
[20] P. Hohenberg, W. Kohn, *Phys. Rev.* **1964**, *136*, B864.
[21] W. Kohn, L. J. Sham, *Phys. Rev.* **1965**, *140*, A1133.
[22] G. Kresse, J. Furthmüller, *Phys. Rev. B* **1996**, *54*, 11169.
[23] G. Kresse, J. Joubert, *Phys. Rev. B* **1999**, *59*, 1758.
[24] http://www.vasp.at/.
[25] J. P. Perdew, K. Burke, M. Ernzerhof, *Phys. Rev. Lett.* **1996**, *77*, 3865.
[26] D. M. Ceperley, B. J. Alder, *Phys. Rev. Lett.* **1980**, *45*, 566.
[27] W. H. Press, B. P. Flannery, S. A. Teukolsky, W. T. Vetterling, *Numerical Recipes*, Cambridge University Press, New York, **1986**.
[28] P. E. Blöchl, *Phys. Rev. B* **1994**, *50*, 17953.
[29] P. E. Blöchl, O. Jepsen, O. K. Andersen, *Phys. Rev. B* **1994**, *49*, 16223.
[30] M. Methfessel, A. T. Paxton, *Phys. Rev. B* **1989**, *40*, 3616.
[31] A. R. Williams, J. Kübler, C. D. Gelatt, Jr., *Phys. Rev. B* **1979**, *19*, 6094.
[32] V. Eyert, *The Augmented Spherical Wave Method – A Comprehensive Treatment*, Lecture Notes in Physics, Springer, Heidelberg **2007**.
[33] R. Hoffmann, *Angew. Chem., Int. Ed. Engl.* **1987**, *26*, 846.
[34] R. Dronskowski, P. E. Blöchl, *J. Phys. Chem.* **1993**, *97*, 8617.
[35] G. Bester, M. Fähnle, *J. Phys.: Condens. Matter* **2001**, *13*, 11541.
[36] J. Emsley, *The Elements*, Oxford University Press, Oxford **1999**.
[37] J. Donohue, *The Structures of the Elements,* Wiley, New York **1974**.
[38] P. Eckerlin, H. J. Meyer, E. Wölfel, *Z. Anorg. Allg. Chem.* **1955**, *281*, 322.
[39] Y. Kubota, M. C. Sison Escaño, H. Nakanishi, H. Kasai, *J. Appl. Phys.* **2007**, *102*, 053704.
[40] S. F. Matar, R. Pöttgen, N. Quaini, *Solid State Sci.* **2012**, *14*, 375.
[41] U.-Ch. Rodewald, R.-D. Hoffmann, Z. Wu, R. Pöttgen, *Z. Naturforsch.* **2006**, *61b*, 108.
[42] R. F. W. Bader, *Chem. Rev.* **1991**, *91*, 893.
[43] N. Li, C. R. Martin, *J. Electrochem. Soc.* **2001**, *148*, A164.
[44] J. Cabana, L. Monconduit, D. Larcher, M. Rosa Palacín, *Adv. Mater.* **2010**, *22*, E170.
[45] W. Weppner, R. A. Huggins, *J. Electrochem. Soc.* **1977**, *124*, 1569.